https://doi.org/10.5194/wes-2026-131
Preprint. Discussion started: 17 August 2026

WIND ENERGY SCIENCE DISCUSSIONS

Reduced-Order Modelling of Nonlinear Wind Turbine Blade Vibrations in a High-Fidelity Unsteady Aeroelastic Framework

Jimmy X. Gan[1], Joaquin E. Moran[1], David A. Romero[1], Cristina H. Amon[1,2*]

[1] Mechanical and Industrial Engineering, University of Toronto, Toronto, M5S 3G8, Canada
[2] Chemical Engineering and Applied Chemistry, University of Toronto, Toronto, M5S 3E5, Canada

Correspondence to: Cristina H. Amon (cristina.amon@utoronto.ca)

Abstract. Accurate modelling of nonlinear wind turbine blade dynamics is essential for the reliable design and operation of modern wind turbines. Wind turbine blades have complex shapes with spatially varying sectional properties, twists and curvatures. The dynamics of long, flexible blades are strongly influenced by geometric nonlinearities, centrifugal effects, and material anisotropies. Conventional linear beam models are inadequate for capturing these complexities, since they are not designed to handle large deformations and nonlinear couplings. This study presents a high-fidelity nonlinear reduced-order model (ROM) for predicting the structural dynamics of modern wind turbine blades. The ROM uses a biorthogonal modal basis derived from the intrinsic mixed formulation of geometrically exact beam theory. The structural model is coupled to a high-fidelity unsteady vortex lattice solver in a two-way fluid-structure interaction framework, improving on the traditional blade element momentum method. The proposed model was validated using numerical and experimental results from the NREL 5-MW and SNL CX-100 wind turbine blades. Benchmark tests demonstrate that the ROM successfully captures the wind turbine blade's nonlinear frequency response to harmonic loads and dynamic response to transient loads, including extreme wind gust, wind shear, and turbulence. Among the wind load cases tested, the ROM's maximum out-of-plane tip displacement error was 0.77% of reference tip deflection, compared with 20.90% for conventional linear time-invariant models. This framework has applications in wind turbine control, structural health monitoring, fatigue life studies, and digital twins.

Abbreviations

Table 1 List of abbreviations

Abbreviation	Description
EOG	Extreme Operating Gust
EWS	Extreme Wind Shear
ETM	Extreme Turbulence Model
FOM	Full-Order Model
GEBT	Geometrically Exact Beam Theory

https://doi.org/10.5194/wes-2026-131
Preprint. Discussion started: 17 August 2026

IGEBT	Intrinsic Geometrically Exact Beam Theory
LTI	Linear Time-Invariant
ROM	Reduced-Order Model
SHARPy	Simulation of High Aspect Ratio Planes in Python
UVLM	Unsteady Vortex Lattice Method

Nomenclature

25 **Table 2 List of symbols**

Symbol	**Definition**
i, j, k	Element indices; $i, j, k \in \{1, \cdots, n\}$
r, s, t	Polynomial order indices; $r, s, t \in \{1, \cdots, m\}$
V	Linear velocity
Ω	Angular velocity
F	Internal force
M	Internal moment
P	Linear momentum
H	Angular momentum
γ	Linear strain
κ	Rotational strain
k	Twist and curvature per unit length
f^{ext}	External forces
m^{ext}	External moments
C^{BA}	Transformation matrix from global frame A to local frame B
C^{AG}	Transformation matrix from inertial frame G to global frame A
g	Gravity vector
q	Generalized coordinates
x	Spatial coordinate along the blade reference line
Φ	Shifted Legendre basis function
U	Direct eigenvector basis function
W	Adjoint eigenvector basis function
η	Modal coordinates

https://doi.org/10.5194/wes-2026-131
Preprint. Discussion started: 17 August 2026

$(\cdot)'$	Spatial derivative with respect to the blade reference line
$\dot{(\cdot)}$	Time derivative
$\widetilde{(\cdot)}$	Skew-symmetric operator
$\widehat{(\cdot)}$	Perturbed quantity
$(\cdot)^r$	Reduced model

1 Introduction

Global demand for wind power is increasing rapidly, with installed capacity projected to grow at 5.2%, or 194 GW, each year from 2026 to 2030 (Gwec, 2026). To meet rising electricity demand, wind farms are built on a wide variety of sites, including complex terrains, offshore locations, and high-turbulence locations in tightly packed layouts. Wind turbines operate under intense wind flow environments, including high wind speeds, atmospheric and wake turbulence, transient wind loads, and frequent wind direction changes (Fig. 1). Traditional analytical flow field models oversimplify unsteady and spatially varying flows, resulting in inaccurate power and load predictions (Porte-Agel et al., 2020). High-fidelity surrogate modelling of wind farm flow fields is a growing research topic, including the use of adjoint methods (Antonini et al., 2020) and machine learning (Romero et al., 2024; Hasanpoor et al., 2025). Concurrently, wind turbines are trending toward larger rotor diameters due to their higher power output and lower cost per MW. From 2012 to 2025, the largest wind turbines have increased from 6 MW with 73.5 m-long blades to 26 MW with 153 m-long blades currently under testing (Alstom, 2012; Dongfang, 2024). In deep-water offshore wind farms, wind turbines are built on floating spars or platforms, whose wave-induced motions strongly influence wind turbine blade dynamics. These trends pose a great challenge for modern wind turbine blade design and operation. Wind turbine blades are flexible, light-weight composite structures with high aspect ratios and can deflect by more than 10% of their span during operation. Due to intense cyclic wind loads, fatigue has become the leading cause of blade failure (Dai et al., 2022; Machado and Dutkiewicz, 2024). Poor wind turbine reliability results in safety and environmental hazards, high maintenance costs, reputational damage, and financial losses from downtime.

As wind turbine blades become longer, lighter, and slenderer, their dynamics are increasingly influenced by geometric nonlinearities. Under large deflections, the relation between applied force and strain becomes nonlinear due to the dependency of the blade's effective stiffness, inertia distribution, and internal load path on its deformed shape (Palacios and Cesnik, 2023). Several studies have compared geometrically nonlinear models to linear models of wind turbine blades. Manolas et al. (Manolas et al., 2015) found a more than 100% increase in torsional moment in a NREL 5-MW wind turbine blade due to nonlinear flexural-torsional coupling. Qu et al (Qu et al., 2020) found that geometrically nonlinear effects increased the blade root lifetime fatigue damage for a 10-MW wind turbine in almost all wind load cases studied. Wang et al (Wang et al., 2026) found a 13.9% difference in maximum flapwise blade deflection and 13.6% difference in out-of-plane aerodynamic loads between linear and nonlinear models for a 15MW wind turbine operating at rated wind speed.

https://doi.org/10.5194/wes-2026-131
Preprint. Discussion started: 17 August 2026

eawe european academy of wind energy
Open Access
WIND ENERGY SCIENCE
DISCUSSIONS

Figure 1: a) Offshore 6-MW wind turbines with 73.5 m-long blades (photo by Dennis Schroeder, NLR/DOE), b) blade failure in a generic wind turbine (photo by Dietmar Händel, CC BY 2.0 license).

Modern wind turbine blades have complex cross-sectional shapes with axial twists and curvatures, spatially varying blade properties, and anisotropies such as passive twist-bend coupling. Three prevalent beam theories used for modelling wind turbine blades are the linear Euler-Bernoulli, Timoshenko, and geometrically exact beam theory (GEBT) (Rafiee et al., 2017). Linear Euler-Bernoulli beam theory assumes that cross sections remain perpendicular to the beam centreline and uses small angle approximation for deflections. Therefore, it cannot model large beam rotations associated with geometric nonlinearities. Timoshenko beam theory can model cross-sectional rotations with respect to the centreline but is limited to small rotation angles. Large rotations can be modelled in the floating frame of reference formulation by superimposing small elastic Timoshenko deformations onto large rigid-body motions. However, the decoupling of elastic and rigid-body motion may lead to inaccuracies for highly nonlinear dynamic cases (Shabana, 1997). To address the geometric limitations of linear beam and multibody methods, GEBT was developed from the nonlinear rod theories of Reissner (Reissner, 1973) and later extended to a three-dimensional finite element framework by Simo and Vu-Quoc (Simo and Vu-Quoc, 1988). GEBT is a Hamiltonian reference line model based on a deforming space curve with rigid sliding cross-sections translating and rotating independently. It can be formulated in terms of global displacements (displacement-based) or local strains (intrinsic mixed formulation) (Palacios and Cesnik, 2023). Unlike linear beam theories, GEBT can model arbitrarily large displacements and rotations in the elastic range. As wind turbine blades become longer and more flexible, an increasing number of wind turbine simulators use GEBT (e.g. SHARPy (Del Carre et al., 2019) and Beamdyn (Wang et al., 2015)).

Reduced-order models (ROM) of wind turbine dynamics play a critical role in wind turbine control, structural health monitoring, fatigue life studies, and digital twins. Full-order GEBT solvers such as SHARPy and BeamDyn are too computationally expensive for real-time state estimation. For these applications, model reduction must be performed. Displacement-based GEBT, due to its high dimensionality and high-order nonlinearity from tracking global rotations, is

https://doi.org/10.5194/wes-2026-131
Preprint. Discussion started: 17 August 2026

typically reduced using Taylor-based methods. A linear time-invariant (LTI) model of wind turbine blade dynamics can be produced by taking a first-order Taylor expansion about a steady state operating point and then reduced via modal projection or moment matching (Hesse and Palacios, 2012; Jonkman et al., 2018). Additionally, higher-order Taylor expansion terms can be retained to produce a nonlinear ROM (Gözcü et al., 2023). However, Taylor-based methods are only accurate for small perturbations about the steady state because the global inertia, stiffness, and damping properties, which are configuration-dependent, become constant upon linearization.

The intrinsic GEBT (IGEBT) formulation has been studied in several recent wind turbine aeroelasticity research papers (Wang et al., 2026; Wang et al., 2025). However, these studies do not address the model order reduction of IGEBT for control and digital twin applications. IGEBT is convenient for nonlinear model order reduction due to its frame invariance and low-order (quadratic) nonlinearity (Hodges, 2003). Its governing equations can be projected onto a reduced basis to create a quadratically nonlinear ROM. Even with a linear basis, the ROM can capture large deformations due to the use of local strain coordinates. Several methods can be used to produce a reduced-order basis. Frequency-based methods, such as the harmonic balance method, project the system onto a truncated Fourier basis (Siami and Nitzsche, 2023). These methods are mainly suited for periodic steady-state dynamic responses to harmonic loads and are less effective for transient responses to arbitrary loads such as wind gusts and turbulence. To address this limitation, recent frameworks have utilized signal windowing functions to condition non-periodic loads and boundary conditions for the Fourier transform (Pamfil et al., 2026). Data-driven methods such as proper orthogonal decomposition extract energy modes from a given dataset using singular value decomposition (Peters et al., 2023; Baisthakur and Fitzgerald, 2025). While highly versatile, data-driven methods can exhibit limited generalization outside the training bounds. Eigen-based methods compute the natural vibration modes of the blade linearized at a steady state operating point (Artola et al., 2022; Althoff et al., 2012). Natural modes offer strong generalizability around the steady state and can be further extended with nonlinear normal modes or modal derivatives to cover a wider operating regime (Palacios, 2011; Wu et al., 2019). However, these additions can significantly increase the computational cost of the model.

Current wind turbine control design largely relies on LTI models to approximate the blade's structural dynamics (Jonkman et al., 2018; Wright and Fingersh, 2008). This study proposes a nonlinear ROM created by projecting the IGEBT equations onto the vibration modes of the blade. To the authors' knowledge, IGEBT-based ROMs for wind turbine blade dynamics has not yet been studied in research literature. Several challenges are associated with this approach. First, the natural vibration modes taken about a rotating steady state are non-orthogonal and coupled due to gyroscopic effects. The resulting truncated modal basis can result in inaccurate forced-response and frequency-response predictions (Genta, 2005). Second, the vibration modes of a wind turbine blade cannot be obtained analytically due to its spatially varying material properties and geometry, necessitating finite element discretization of the IGEBT equations. The goal of this study is to produce a highly accurate and computationally efficient ROM that captures the nonlinear dynamics of a real operational wind turbine blade subjected to unsteady and unevenly distributed loads. The three main contributions of this paper are:

1. The formulation of a compact hierarchical spectral finite element discretization of the IGEBT equations for a realistic, spatially varying wind turbine blade. In subsequent text, this model will be referred to as the full-order model (FOM).

https://doi.org/10.5194/wes-2026-131
Preprint. Discussion started: 17 August 2026

2. The formulation of a robust, spectrally accurate reduced-order model (ROM) of the IGEBT equations using linearly independent biorthogonal vibration modes for a rotating wind turbine blade. In subsequent text, this model will be referred to as the ROM.
3. Validation of the biorthogonal ROM by comparing with experimental measurements available in the literature (Paquette et al., 2011; Farinholt et al., 2012), and benchmarking its performance against conventional LTI and modal reduction methods using advanced frequency response analysis and transient wind load cases applied in a high-fidelity, two-way aeroelastic framework.

Numerical benchmarks were based on SHARPy, an open source aeroelastic software developed and extensively validated by Imperial College London (Del Carre et al., 2019). SHARPy uses a displacement-based GEBT solver for modelling structural dynamics and an unsteady vortex lattice method (UVLM) solver for computing aerodynamic loads. This solver has been extensively benchmarked against OpenFAST and actuator line method simulations (Muñoz-Simón, 2021). To test its performance under realistic wind loads, the ROM was tightly coupled to SHARPy's UVLM solver in a two-way aeroelastic framework. Realistic load cases based on standard IEC 61400-1 were used in the performance assessment.

2 Structural Model

IGEBT is a Hamiltonian system derived from momentum balance and intrinsic kinematic equations of a body in motion. It describes the nonlinear dynamics of beams with arbitrary cross-sections, material properties, twists and curvatures. This study models the wind turbine blades as cantilever beams rotating at a prescribed angular velocity. This study will focus on the dynamics of the wind turbine blade, excluding from the formulation the response of the nacelle and tower. In addition, structural damping is neglected due to the low damping ratio of wind turbine blades (Jonkman et al., 2009; Paquette et al., 2011).

2.1 IGEBT Equations

The IGEBT equations are expressed in terms of linear velocity V, angular velocity Ω, internal force F, and internal moment M coordinates in the deformed local frame B (Fig. 2) (Hodges, 2003). Equations 1 and 2 are the equations of motion of the blade derived from momentum balance, while Equations 3 and 4 are the intrinsic kinematic equations derived from the generalized strain-displacement and velocity-displacement relations as follows:

$$F' + \left(\tilde{k} + \tilde{\kappa}\right)F + f^{ext} = \dot{P} + \tilde{\Omega}P, \tag{1}$$

$$M' + \left(\tilde{k} + \tilde{\kappa}\right)M + (\tilde{e}_1 + \tilde{\gamma})F + m^{ext} = \dot{H} + \tilde{\Omega}H + \tilde{V}P, \tag{2}$$

$$V' + \left(\tilde{k} + \tilde{\kappa}\right)V + (\tilde{e}_1 + \tilde{\gamma})\Omega = \dot{\gamma}, \tag{3}$$

$$\Omega' + \left(\tilde{k} + \tilde{\kappa}\right)\Omega = \dot{\kappa}, \tag{4}$$

https://doi.org/10.5194/wes-2026-131
Preprint. Discussion started: 17 August 2026

where γ and κ are the linear and rotational strains, respectively, P and H are the linear and angular momentums, respectively,
135 k is the twist and curvature per unit length, e_1 is the unit vector [1,0,0], f^{ext} and m^{ext} are the external forces and moments, respectively. Here, $(\cdot)'$ denotes the spatial derivative with respect to the blade reference line and $\widetilde{(\cdot)}$ is a skew-symmetric operator. The strain (γ, κ) and momentum (P, H) terms are related to the intrinsic mixed coordinates $(V, \Omega, \mathrm{F}, \mathrm{M})$ through the 6×6 cross-sectional stiffness and mass matrices along the blade, i.e.,

$$\begin{Bmatrix} \gamma \\ \kappa \end{Bmatrix} = \begin{bmatrix} R(x) & S(x) \\ S(x)^T & T(x) \end{bmatrix} \begin{Bmatrix} F \\ M \end{Bmatrix}, \tag{5}$$

$$\begin{Bmatrix} P \\ H \end{Bmatrix} = \begin{bmatrix} \mu(x)\mathrm{I}_3 & -\mu(x)\tilde{\xi}(x) \\ \mu(x)\tilde{\xi}(x) & I(x) \end{bmatrix} \begin{Bmatrix} V \\ \Omega \end{Bmatrix} = \begin{bmatrix} G(x) & K(x) \\ K(x)^T & I(x) \end{bmatrix} \begin{Bmatrix} V \\ \Omega \end{Bmatrix}, \tag{6}$$

where x is the spatial coordinate along the blade reference line, R, S, T are the 3×3 cross-sectional flexibility coefficient
140 matrices, μ is the mass per unit length, ξ is the mass centre offset of the cross-section from the reference line, I is the mass moment of inertia per unit length, and I is the identity matrix.

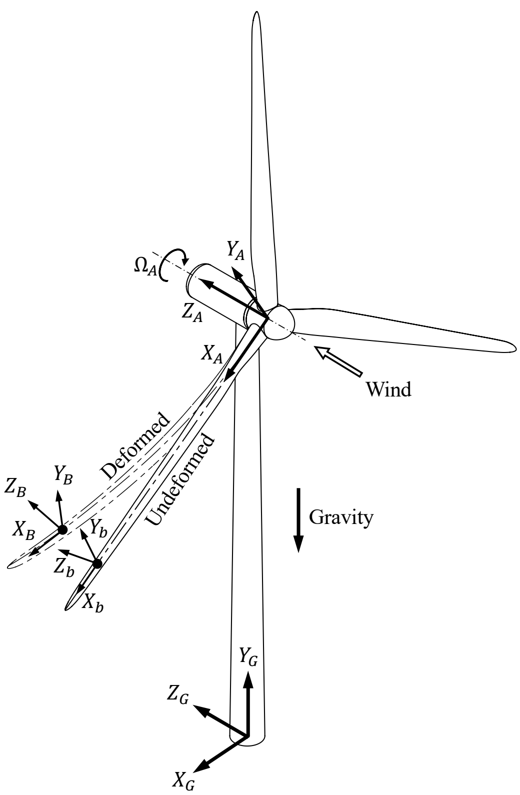

Figure 2: Reference frames used for coordinate conversion: G is inertial frame, A is global frame, b is undeformed local frame, B is local frame (material frame).

145 In this study, the flapwise (Z_B) and edgewise (Y_B) directions refer to the directions perpendicular and parallel to the local blade chord, respectively. The out-of-plane (Z_A) and in-plane ($X_A Y_A$) directions refer to the directions normal and tangential to

https://doi.org/10.5194/wes-2026-131
Preprint. Discussion started: 17 August 2026

the rotor plane, respectively. The intrinsic blade strains in local frame B are converted to global displacements in frame A using the generalized strain-displacement and velocity-displacement relations (Hodges, 2006). Frame A is attached to the rotor hub axis and rotates with the rotor at angular velocity Ω_A (a single frame A is used for the whole rotor). Each wind turbine blade is modelled as a cantilever beam with a prescribed local angular velocity Ω^0 at the blade root.

$$V(0,t) = 0, \qquad \Omega(0,t) = \Omega^0 = C^{BA}\Omega_A, \qquad F(L,t) = F^L, \qquad M(L,t) = M^L, \tag{7}$$

where transformation matrix C^{BA} is governed by the angle of twist and curvature at the blade root. The inertial gravity vector g_G is transformed to the local gravity vector g_B according to the blade's current azimuth angle and local deformed orientation:

$$g_B{}' + \left(\tilde{\kappa} + \tilde{k}\right) g_B = 0, \tag{8}$$

$$g_B^0 = C^{BA} C^{AG} g_G, \tag{9}$$

where transformation matrix C^{AG} is governed by the current azimuth angle of the blade and g_B^0 is the local gravity vector at the blade root. The local gravity vector g_B for the remainder of the blade is solved through forward integration of Equation 8.

2.2 Spatial Discretization

The FOM is created using a hierarchical spectral finite element method, where the IGEBT model of the wind turbine blade is projected onto n spectral elements of order m. Legendre polynomials, shifted from their original range [-1,1] to [0,1] for convenience, are chosen as the basis function due to their orthogonality, smoothness, and exponential convergence properties resulting in highly accurate models. The intrinsic coordinates are represented by Legendre basis functions $\Phi_r(x_i)$ and generalized coordinates $q_{r,i}(t)$:

$$\Phi_r(x_i) = \begin{bmatrix} \mathcal{P}_{r-1}(x_i/L_i) & 0 & 0 \\ 0 & \mathcal{P}_{r-1}(x_i/L_i) & 0 \\ 0 & 0 & \mathcal{P}_{r-1}(x_i/L_i) \end{bmatrix}, \tag{10}$$

$$q_i(t) = [v_{1,i}(t) \quad \omega_{1,i}(t) \quad f_{1,i}(t) \quad m_{1,i}(t) \quad \cdots \quad v_{m,i}(t) \quad \omega_{m,i}(t) \quad f_{m,i}(t) \quad m_{m,i}(t)]^T, \tag{11}$$

where element index $i \in \{1, \cdots, n\}$, polynomial order index $r \in \{1, \cdots, m\}$, x_i is the spatial coordinate along the blade element reference line, L_i is the element length, $\mathcal{P}$ is the shifted Legendre polynomial function, and v, ω, f, m are 3×1 vectors.

A Galerkin projection is performed by replacing the intrinsic state variables with a Legendre trial solution, pre-multiplying the IGEBT equations with each Legendre basis function and integrating over the spatial domain. This procedure transforms the governing partial differential equations into a set of ordinary differential equations (Patil and Hodges, 2011). Physically, the projection yields an energy conservation relation equating the rate of change of the blade's total energy (kinetic and potential) to the rate of work done by external aerodynamic and gravity loads. To evaluate these integrals for a wind turbine blade with spatially varying properties, the Gauss-Legendre quadrature is employed. The resulting discretization is a first-order, quadratically nonlinear ODE in time, with a total size of $N_f = 12mn$ (representing the 6 strain and 6 velocity states).

https://doi.org/10.5194/wes-2026-131
Preprint. Discussion started: 17 August 2026

$$A_{ij}\dot{q}_j + B_{ij}q_j + C_{ijk}q_jq_k + D_i = 0, \tag{12}$$

$$(A_{ij})_{rs} = \mathbb{A}_{rs,i}\delta_{ij}, \tag{13}$$

$$(B_{ij})_{rs} = \mathbb{B}_{rs,i}\delta_{ij} + \mathbb{L}_{rs,i}\delta_{i,j-1} + \mathbb{R}_{rs,i}\delta_{i,j+1}, \tag{14}$$

$$(C_{ijk})_{rst} = \mathbb{C}_{rst,i}\delta_{ij}\delta_{ik}, \tag{15}$$

$$(D_i)_r = \mathbb{D}_{r,i}, \tag{16}$$

where $r, s, t \in \{1, \cdots, m\}$ and $i, j, k \in \{1, \cdots, n\}$. $\mathbb{A}_{rs,i}$, $\mathbb{B}_{rs,i}$, $\mathbb{C}_{rst,i}$, $\mathbb{D}_{r,i}$, $\mathbb{L}_{rs,i}$, and $\mathbb{R}_{rs,i}$ are elemental submatrix blocks. The detailed expressions for these submatrix blocks are presented in Appendix A. Matrices A_{ij}, B_{ij}, C_{ijk} are constant and computed one time offline. Column vector D_i, which contains external forcing terms, must be updated at each timestep.

2.3 Modal Reduction

For a given set of boundary conditions, the FOM (Equation 12) is reformulated in terms of perturbations ($\hat{q}$) about the steady state solution (q^{ss}). The linearized perturbed system is expressed as:

$$\hat{A}_{ij}\dot{\hat{q}}_j + \hat{B}_{ij}\hat{q}_j = 0, \tag{17}$$

$$\hat{A}_{ij} = A_{ij}, \tag{18}$$

$$\hat{B}_{ij} = B_{ij} + \left(C_{ijk} + C_{ikj}\right)q_k^{ss}. \tag{19}$$

When linearized about a rotating steady state ($q^{ss} \neq 0$), the natural modes of the system are complex and non-orthogonal due to gyroscopic terms. Upon truncation, this coupled modal basis may lead to inaccuracies in forced-response and frequency-response predictions. To obtain a consistent modal representation of the non-self-adjoint system, a biorthogonal modal basis is used (Meirovitch, 1997; Patil, 2000). The direct and adjoint complex eigenvectors (u and w, respectively) are computed from their corresponding eigenvalue problems:

$$\lambda\hat{A}u_p = -\hat{B}u_p, \qquad p = 1, \cdots N_f \tag{20}$$

$$\lambda\hat{A}^T w_p = -\hat{B}^T w_p, \qquad p = 1, \cdots N_f \tag{21}$$

where λ represents the eigenvalues of the linear system. The normalized direct and adjoint eigenvectors expressed in terms of N_f real vectors ($\bar{U}$ and $\bar{W}$, respectively) satisfy the following biorthogonality relations:

$$\bar{W}^T\hat{A}\bar{U} = \mathrm{I}_{N_f}, \tag{22}$$

$$\bar{W}^T\hat{B}\bar{U} = \bar{B}, \tag{23}$$

https://doi.org/10.5194/wes-2026-131
Preprint. Discussion started: 17 August 2026

WIND ENERGY SCIENCE DISCUSSIONS

where $\bar{B}$ is a block diagonal matrix and I is the identity matrix. To produce a reduced basis, $\bar{U}$ and $\bar{W}$ are truncated to N_r real vectors ($N_r \ll N_f$) to form the basis functions $U, W \in \mathbb{R}^{N_f \times N_r}$. The nonlinear ROM is created via a Petrov-Galerkin projection of the perturbed FOM onto this truncated modal basis.

$$A^r \dot{\eta} + B^r \eta + C^r \eta\eta + D^r = 0, \tag{24}$$

$$\hat{q} = U\eta, \tag{25}$$

$$A^r = W^T \hat{A} U, \tag{26}$$

$$B^r = W^T \hat{B} U, \tag{27}$$

$$C^r = W^T \hat{C} (U \otimes U), \tag{28}$$

$$D^r = W^T \hat{D}, \tag{29}$$

Biorthogonality yields a diagonal representation of the linearized dynamics in the full eigenvector basis ($\bar{U}$ and $\bar{W}$), with modes decoupled at the linear level and coupled only through the nonlinear quadratic terms. Upon modal truncation to a reduced subspace (U and W), the projected linear operator remains diagonal in the retained modes. This leads to a ROM in which linear modal interactions are eliminated, allowing nonlinear effects to be isolated more clearly and improving the physical interpretability of the resulting dynamics.

3 Fluid-Structure Interaction

To translate complex wind flow fields into realistic unsteady wind loads on the turbine blade, a UVLM aerodynamic solver is used (Del Carre et al., 2019). UVLM is a potential flow model that assumes inviscid, incompressible, and irrotational conditions. Due to the irrotational assumption, UVLM is not suitable for detached flow modelling (e.g. stall conditions). Since the main operating regime of a wind turbine is attached flow, we deem this approximation appropriate and rely on the UVLM model for our aerodynamic load predictions. UVLM can account for complex flow features, such as unsteady and spatially varying flow fields, spanwise flow effects, wind direction changes, and velocity variations due to turbulence. UVLM is a higher fidelity method than the conventional blade element momentum method, which relies on empirical and analytical correction factors for unsteady and spatially varying flows (Madsen et al., 2011; Rahimi et al., 2016; Madsen et al., 2003). In this study, the SHARPy UVLM solver is used.

In SHARPy, the NREL 5-MW wind turbine blade is discretized into 28 spanwise panels and 8 chordwise panels based on earlier wind turbine studies (Muñoz-Simón et al., 2020; Muñoz-Simón, 2021). This corresponds to 14 quadratic elements along the blade reference line, each with different but constant stiffness and mass properties. For consistency, the same material property distribution was applied to the FOM and ROM. Aerodynamic loads were collocated onto 27 nodes along the blade reference line, with the two hub nodes excluded (Fig. 3 and Fig. 4). Each aeroelastic simulation included three wind turbine

https://doi.org/10.5194/wes-2026-131
Preprint. Discussion started: 17 August 2026

blades with three helicoidal blade wakes. To reduce the computational cost, the wake vortex panel convection was prescribed using the background wind flow only (self-induction was excluded). Studies have shown that the difference in computed aerodynamic loads with and without self-induced wake convection is minimal (Murua et al., 2012; Muñoz-Simón, 2021).

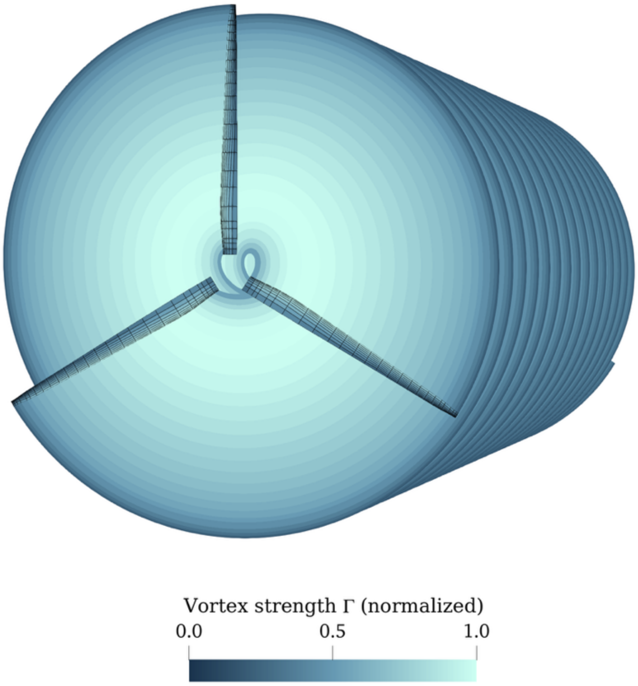

210 **Figure 3: Vortex lattice discretization of the NREL 5-MW wind turbine blades and wake.**

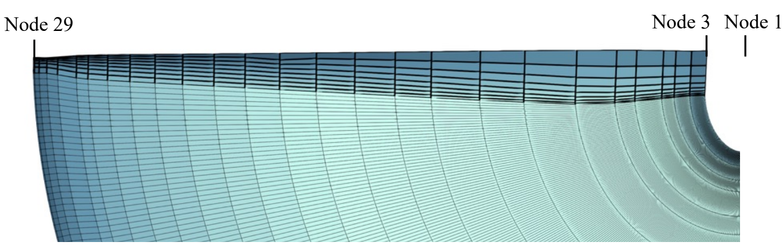

Figure 4: Close-up of vortex lattice discretization for one blade.

The structural model is tightly coupled to a UVLM aerodynamic solver in a two-way aeroelastic framework. The relative wind velocity at the blade surface is governed by the background wind flow, the blade's kinematic velocity, and the upwash / downwash induced by the wake vortices. Based on this relative wind velocity, the UVLM solver outputs the aerodynamic forces and moments at 27 nodes along the blade. At each timestep, the aerodynamic loads, structural deformation, velocities, and blade orientation are updated iteratively until successive blade coordinates converge within 1×10^{-3} m and aerodynamic loads converge within 1×10^{-3} N (Fig. 5). This iterative time stepping process is summarized in Fig. 5.

https://doi.org/10.5194/wes-2026-131
Preprint. Discussion started: 17 August 2026

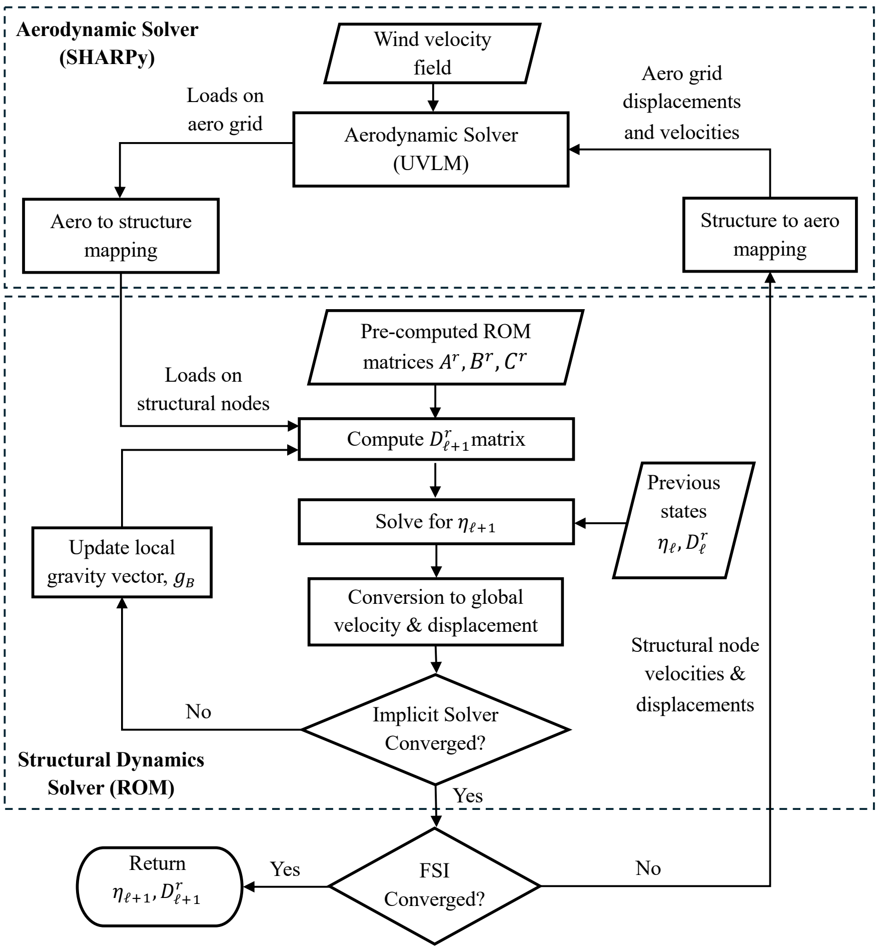

Figure 5: Algorithm for iterative aeroelastic coupling between the fluid mechanics (UVLM) and structural (ROM) components for each timestep ℓ.

4 Test Cases

The FOM solver was first validated against experimental data from static tests on the SNL CX-100 wind turbine blade. Once the FOM solver was validated, a ROM of the NREL 5-MW wind turbine blade dynamics was created using the biorthogonal modal reduction method outlined in Sect. 2. The ROM performance was then benchmarked against full SHARPy simulations. SHARPy was deemed a reliable reference due to its extensive testing and validation against OpenFAST and actuator line methods, including for the NREL 5-MW wind turbine blade (Muñoz-Simón, 2021). A summary of all the tests conducted in this study is presented in Table 3.

https://doi.org/10.5194/wes-2026-131
Preprint. Discussion started: 17 August 2026

Table 3: Summary of test cases used for validation

No.	Test	Blade	Description
1	Static load (Sect. 5.1)	SNL CX-100	The cantilevered blade was pitched at 5.25° and tilted downward such that under full load, the applied forces are perpendicular to the deformed blade (Paquette et al., 2011). The blade was loaded at three locations as indicated in Fig. 6, with a string pot installed at each load saddle to measure the vertical deflection.
2	Modal hammer (Sect. 5.1)	SNL CX-100	The natural frequencies of the cantilevered blade were excited using hammer impacts and recorded with piezoelectric transducers (Farinholt et al., 2012).
3	Frequency response (Sect. 5.2.1)	NREL 5-MW	The nonlinear frequency response of the blade under a harmonic flapwise distributed load of 60 N/m was computed (Bekhoucha et al., 2013). The ROM's frequency response was compared to the FOM.
4	Wind load cases (Sect. 5.2.2)	NREL 5-MW	Three operationally relevant wind load cases from the IEC 61400-1 standard were applied to the ROM and LTI models to compare their performance: extreme operating gust, wind shear, and turbulence. All load cases start from the rated wind speed (11.4 m/s) and include gravity loads. The wind turbine, assumed be IEC 61400-1 Class IA, was set to rated speed (12.1 rpm) and 0° collective blade pitch for the full simulation duration.

The CX-100 is an experimental fiberglass wind turbine blade designed by Sandia National Laboratories (SNL). The blade is 9 m long and has a 29.6° twist. The blade is composed of a glass fibre reinforced epoxy shell with carbon fibre spar caps and a balsa wood shear web (Berry and Ashwill, 2007). The cross-sectional stiffness and mass properties at 40 locations along the blade, derived using asymptotic modelling, were provided by Los Alamos National Laboratory (Fleming and Luscher, 2013).

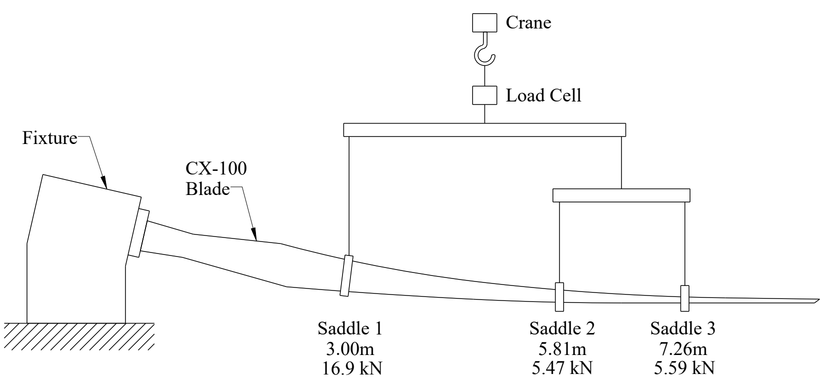

Figure 6: CX-100 blade static load experiment setup.

https://doi.org/10.5194/wes-2026-131
Preprint. Discussion started: 17 August 2026

The NREL 5-MW wind turbine is a theoretical wind turbine designed by the National Laboratory of the Rockies (previously named National Renewable Energy Laboratory, or NREL). This is a widely used reference turbine design for numerical experiments conducted in wind energy research. The basic properties of the NREL 5-MW wind turbine are presented in Table 4.

Table 4: Properties of NREL 5-MW wind turbine (Jonkman et al., 2009)

Tower height	90 m
Rotor, hub diameter	126 m, 3 m
Blade length	61.5 m
Total twist	13.308°
Cut-in, rated, cut-out wind speed	3 m/s, 11.4 m/s, 25 m/s
Rated speed	12.1 rpm

5 Results and Analysis

Based on convergence results from an earlier study, we chose Legendre polynomials of order 10 as the starting point for creating the FOM (Patil and Hodges, 2011). A mesh refinement study concluded that three elements of equal length were required for static convergence and dynamic stability of the wind turbine blade ($n = 3, m = 10$). Subsequently, a ROM basis was derived by linearizing the FOM about a rotating and unloaded state ($\Omega_A = 12.1\ rpm$, rated speed). An LTI model was derived from SHARPy at the same operating point. In time domain simulations, an implicit midpoint algorithm was selected to integrate the ROM due to its second-order accuracy and unconditional stability. A timestep size corresponding to a 0.5° azimuth increment per timestep at rated rotation speed (approximately 6.9×10^{-3} seconds) was used for all cases. To simulate wind loads, both the ROM and LTI models were coupled to the UVLM aerodynamic solver in the two-way aeroelastic framework presented in Sect. 3.

5.1 Experimental Validation and Benchmarking

The results of the static and hammer benchmark tests on the SNL CX-100 wind turbine blade are presented in Fig. 7 and Table 5. The FOM blade deflections match very well with experimental results at the first two saddles, but diverge slightly at the third saddle, with a maximum difference of 0.072 m (11.4%) compared with the experimental deflection. The static results from the FOM closely match published numerical data from NREL's BeamDyn solver, which also concluded that the experimental blade is slightly stiffer in the flapwise direction than the numerical model (Wang et al., 2015). It is noteworthy that these numerical models used the same blade cross-sectional data. In the impact hammer test, the average difference in the first eight natural frequencies between FOM and experimental results is 4.5%. In both tests, the FOM result is an almost exact match with SHARPy.

https://doi.org/10.5194/wes-2026-131
Preprint. Discussion started: 17 August 2026

WIND ENERGY SCIENCE DISCUSSIONS

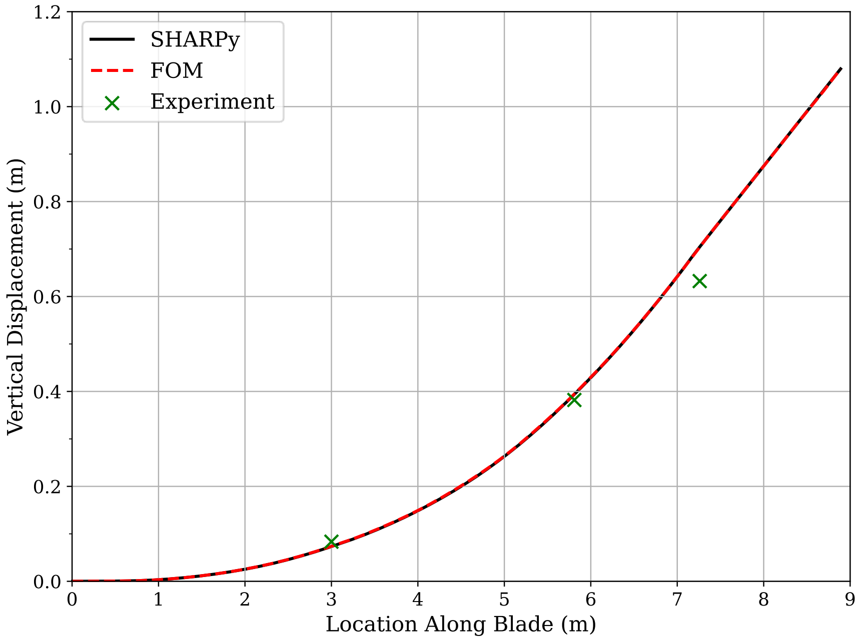

265 **Figure 7. Comparison of CX-100 blade deflection along span between FOM, SHARPy, and experiment (Paquette et al., 2011).**

Table 5: Benchmark of CX-100's natural frequencies (Farinholt et al., 2012)

Description	Type	Experiment (Hz)	FOM (Hz) / %[1]	SHARPy (Hz) / %[1]
Mode #1	Flapwise	4.35	4.85 (11.5%)	4.85 (11.5%)
Mode #2	Edgewise	6.43	5.85 (9.0%)	5.87 (8.7%)
Mode #3	Flapwise	11.51	12.85 (11.6%)	12.89 (12.0%)
Mode #4	Flapwise	20.54	20.31 (1.1%)	20.37 (0.8%)
Mode #5	Edgewise	23.11	25.68 (11.1%)	25.79 (11.6%)
Mode #6	Flapwise	35.33	40.30 (14.1%)	40.46 (14.5%)
Mode #7	Torsion	46.27	46.18 (0.2%)	46.24 (0.1%)
Mode #8	Edgewise	48.64	47.62 (2.1%)	47.78 (1.8%)

Note 1: Percent difference compared with experimental results.

5.2 Performance Evaluation

The ROM's performance under dynamic loads was benchmarked against SHARPy simulations based on frequency and time-
270 domain tests on the NREL 5-MW wind turbine blade.

https://doi.org/10.5194/wes-2026-131
Preprint. Discussion started: 17 August 2026

5.2.1 Modal Analysis

The results for the natural frequencies of the FOM and SHARPy models in both stationary and rotating configurations match well. The modes and natural frequencies were computed using the generalized Schur decomposition method. The first six modes are shown in Table 6.

275 **Table 6: NREL 5-MW wind turbine blade modelled natural frequencies**

	$\Omega_A = 0$ rpm				$\Omega_A = 12.1$ rpm			
Description	**Type**	**FOM (Hz)**	**SHARPy (Hz)**	**% Diff.**	**Type**	**FOM (Hz)**	**SHARPy (Hz)**	**% Diff.**
Mode #1	Flapwise	0.669	0.676	1.0%	Flapwise	0.721	0.727	0.9%
Mode #2	Edgewise	1.072	1.080	0.7%	Edgewise	1.080	1.087	0.7%
Mode #3	Flapwise	1.920	1.951	1.6%	Flapwise	1.979	2.009	1.5%
Mode #4	Edgewise	3.805	3.855	1.3%	Edgewise	3.825	3.876	1.3%
Mode #5	Flapwise	4.349	4.435	1.9%	Flapwise	4.403	4.489	1.9%
Mode #6	Torsion	5.712	5.720	0.1%	Flapwise	5.716	5.724	0.1%

A frequency response analysis was performed using four harmonics (Fig. 8), consistent with the typical ranges in literature (Bekhoucha et al., 2013), and was found to provide converged results in the present study. To obtain representations of the FOM and ROM in Fourier space, the harmonic balance method was used. The frequency response curves were then computed using the pseudo-arclength method. A convergence study concluded that a minimum of 20 biorthogonal modes were required to approximate the nonlinear frequency response of the FOM (Fig. 9a). The performance of the biorthogonal modes stands in contrast with that of direct modes, which exhibit a distorted frequency response. On the other hand, the LTI model, which cannot capture geometric nonlinearity, is represented by a vertical line at the natural frequency. To assess the effect of modal truncation on time-domain accuracy, a convergency study was done on the steady state velocity error of the rotating blade tip under a steady 11.4 m/s wind load (Fig. 9b). At steady state, the velocity of the blade tip relative to the rotating global frame A should be zero, and any non-zero velocity constitutes an error. The convergence results show that when the modal basis is small (<12 modes), biorthogonal modes achieve a lower steady state velocity error than direct modes. Beyond this level, both models achieve a similar degree of accuracy under steady state loading.

https://doi.org/10.5194/wes-2026-131
Preprint. Discussion started: 17 August 2026

WIND ENERGY SCIENCE DISCUSSIONS
Open Access

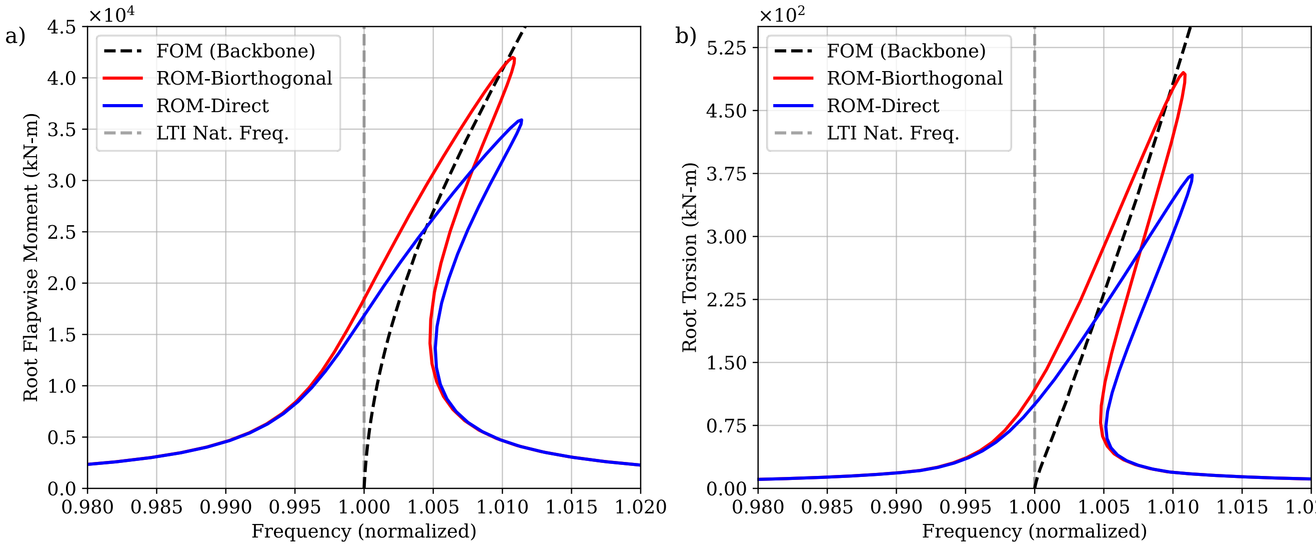

Figure 8: Frequency response under a 60 N/m harmonic distributed flapwise force for the FOM backbone curve (locus of resonance peaks), ROM (biorthogonal modes), and ROM (direct modes) at the first natural frequency. a) Root flapwise bending moment, b) root torsion.

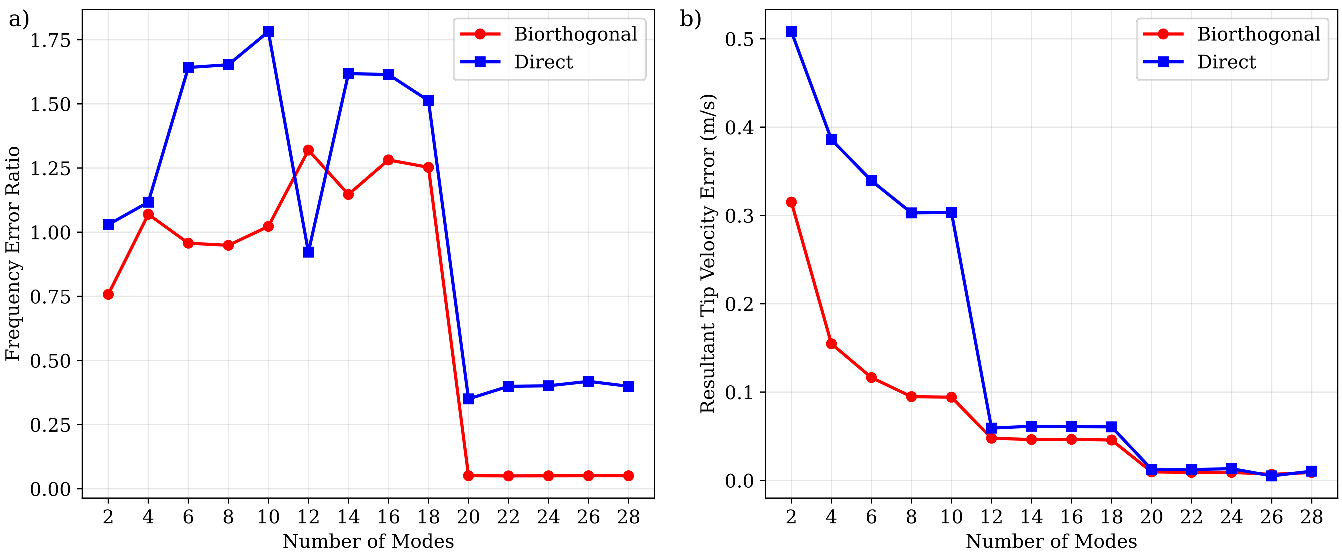

Figure 9: Modal truncation convergence analysis for biorthogonal and direct modes. a) Frequency error at the ROM's resonance peak relative to the FOM backbone, b) steady state tip velocity error relative to rotating global frame *A*.

5.2.2 Transient Wind Load Cases

The transient wind load cases adapted from IEC 61400-1 are summarized in Table 7 and focus on the out-of-plane displacements and torsional deformations of the blade. Out-of-plane tip displacements are induced by normal wind forces, which constitute the largest and most critical load direction. On the other hand, torsional deformation strongly influences the angle of attack and aerodynamic loads in the coupled aeroelastic system. In-plane displacements are not included as they are

https://doi.org/10.5194/wes-2026-131
Preprint. Discussion started: 17 August 2026

mainly influenced by gravity rather than aerodynamic loads. The time histories of the out-of-plane tip displacement (Z_A direction) and torsional tip deformation (X_A direction) are plotted in Figs. 10 to 12, with maximum errors summarized in Table 8.

Table 7: Load cases tested.

Load case	Description	Start time
EOG	Wind gust with an amplitude of +4.2 m/s and a total duration of 10.5s, as defined in IEC 61400-1.	$t = 8\ s$
EWS	Wind shear disturbance superimposed on a steady wind profile (power exponent = 0.2) over a period of 12 seconds, as defined in IEC 61400-1.	$t = 8\ s$
ETM	Von Karman turbulence with a reference intensity of $I_{ref} = 0.16$ and longitudinal standard deviation of $\sigma = 3.51$, as defined in IEC 61400-1. As a simplifying assumption, the wind profile is uniform across the rotor face with wind speed fluctuations occurring in the streamwise direction only.	$t = 0\ s$

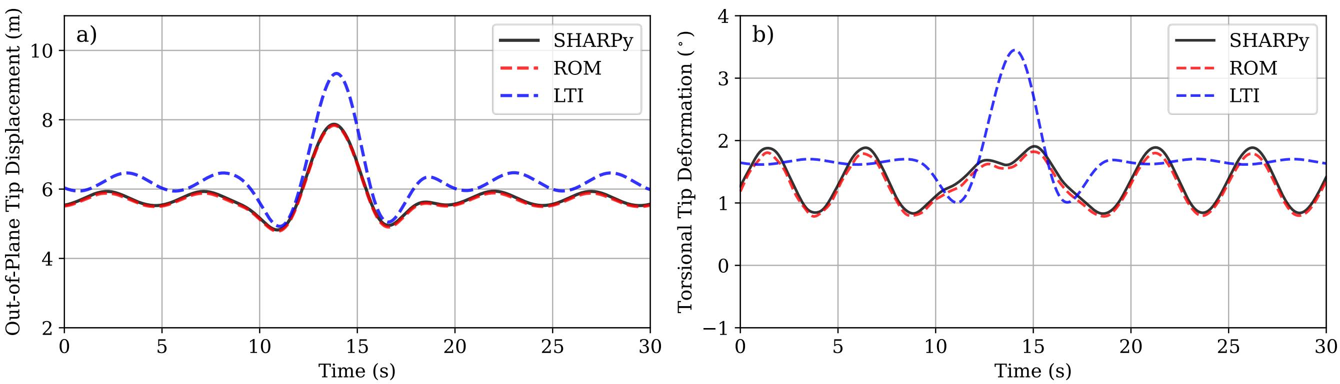

Figure 10: EOG response: SHARPy baseline, ROM, and LTI. a) Out-of-plane tip displacement, b) torsional tip deformation.

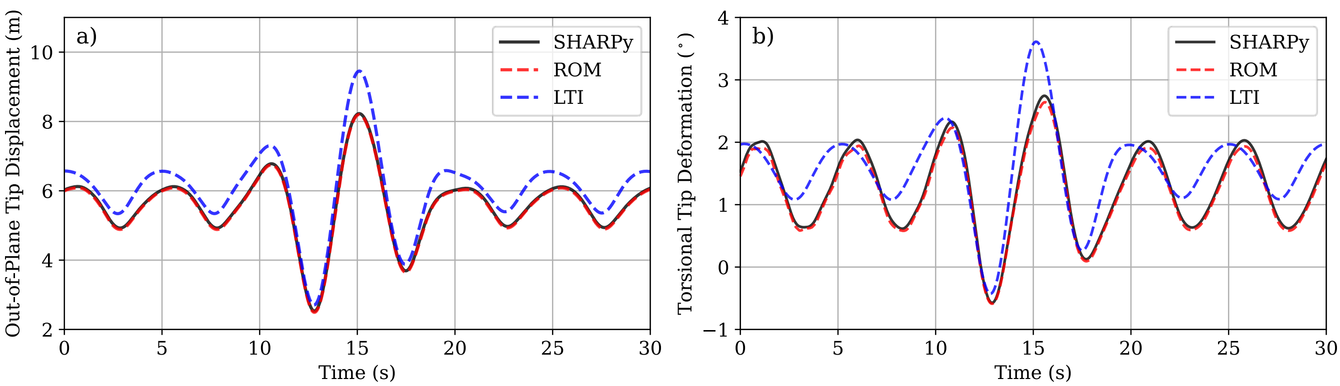

Figure 11: EWS response: SHARPy baseline, ROM, and LTI. a) Out-of-plane tip displacement, b) torsional tip deformation.

https://doi.org/10.5194/wes-2026-131
Preprint. Discussion started: 17 August 2026

WIND ENERGY SCIENCE DISCUSSIONS

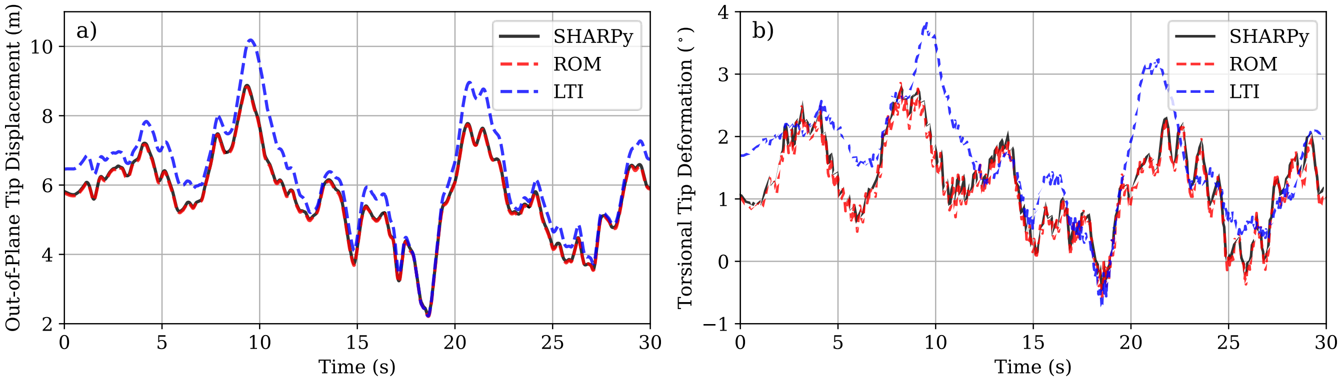

Figure 12: ETM response: SHARPy baseline, ROM, and LTI. a) Out-of-plane tip displacement, b) torsional tip deformation.

Table 8: Comparison table for maximum errors of ROM and LTI compared with SHARPy.

Load Case	Out-of-Plane Displacement Max. Error (m) / %[1]		Torsional Deformation Max. Error (°) / %[1]	
	ROM	LTI	ROM	LTI
Steady	0.051 (0.86%)	0.76 (12.87%)	0.11 (5.87%)	0.85 (45.25%)
EOG	0.052 (0.66%)	1.50 (19.07%)	0.11 (6.03%)	1.80 (94.14%)
EWS	0.048 (0.59%)	1.23 (14.91%)	0.13 (4.59%)	1.23 (44.66%)
ETM	0.068 (0.77%)	1.86 (20.90%)	0.29 (10.26%)	1.89 (66.68%)

Note 1: Percent difference compared with maximum deformation in SHARPy.

The results generally show that the ROM outperforms the LTI model in time response predictions. Due to two-way aeroelastic coupling, structural dynamics errors compound with aerodynamic load errors. Table 9 shows the aerodynamic coefficient errors of the ROM and LTI models under a constant wind speed of 11.4 m/s during one full blade revolution and under the wind gust load case (Fig. 13).

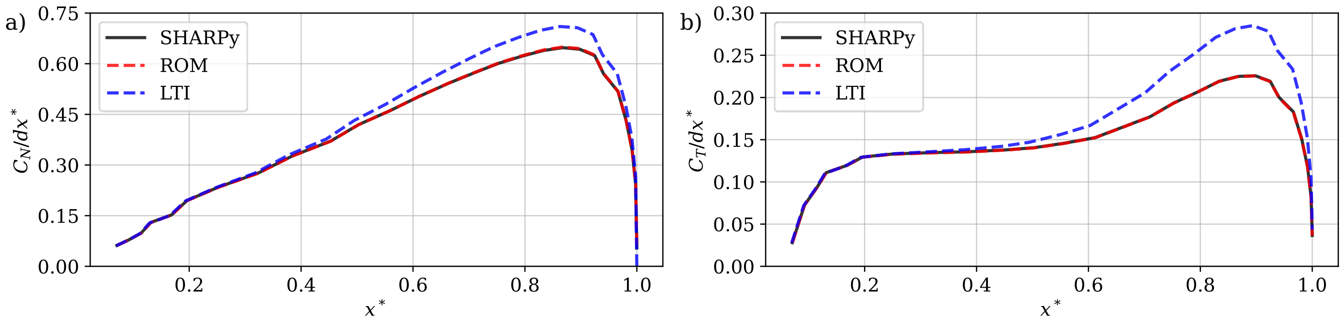

Figure 13: Comparison of blade coefficients along the normalized blade span at EOG peak between SHARPy baseline, ROM, and LTI: a) Out-of-plane, b) in-plane.

https://doi.org/10.5194/wes-2026-131
Preprint. Discussion started: 17 August 2026

Table 9: Aerodynamic coefficient errors during steady state (one full blade revolution) and EOG wind load case.

	Out-of-Plane Coefficient Error / %		In-Plane Coefficient Error / %	
	ROM	LTI	ROM	LTI
Steady wind	Max.: 1.50e-3 (0.36%) MAE: 8.95e-4 (0.21%)	Max.: 4.44e-2 (9.40%) MAE: 2.39e-2 (4.99%)	Max.: 1.16e-3 (1.02%) MAE: 8.33e-4 (0.77%)	Max.: 2.47e-2 (21.97%) MAE: 1.52e-2 (13.02%)
EOG	Max.: 2.33e-3 (0.37%) MAE: 9.23e-4 (0.22%)	Max.: 7.44e-2 (11.75%) MAE: 2.58e-2 (5.19%)	Max.: 6.22e-4 (0.35%) MAE: 7.98e-4 (0.75%)	Max.: 6.47e-2 (30.97%) MAE: 1.72e-2 (13.47%)

Note 1: Percent difference compared with SHARPy results. MAE is mean absolute error for the simulation duration.

6 Discussion

The FOM and ROM were successfully validated with experimental and numerical benchmarks. The static and modal tests on the SNL CX-100 blade showed that the hierarchical spectral finite element discretization of the FOM successfully captures the spatial variations and vibration modes of the wind turbine blade. FOM agreed very well with numerical simulation results from SHARPy and BeamDyn, but all three models exhibited modest deviations from experimental static test data at Saddle #3 (Fig. 7). Given the uncertainties in experimental testing of the blade, including potential discrepancies in the rigidity of boundary conditions, load/sensor orientation, and assumed material properties, it can be concluded that the FOM performed reasonably well against experimental data.

A ROM of the NREL 5-MW wind turbine blade was created using 20 biorthogonal vibration modes, constituting an approximately 90% reduction of the FOM system size. The inclusion of the first axial vibration mode (mode 20) significantly improved the frequency response accuracy by capturing the radial foreshortening effects under large vibration amplitudes. The frequency response analysis indicated that the biorthogonal ROM accurately approximates the dynamic stiffening behaviour of the FOM in the load cases tested (Fig. 8). Physically, this nonlinearity stems from the increased effective structural stiffness associated with large blade strains. In contrast, the direct modal basis of the same size exhibits a distorted frequency response due to its non-orthogonality and coupled modes. The superior accuracy of biorthogonal modes near blade resonance may prove useful for stability analysis and control-oriented model order reduction (Svendsen et al., 2011). However, it is noteworthy that both biorthogonal and direct modal bases are linear and hence cannot evolve along the full system's invariant manifold. At extreme resonance peaks, the biorthogonal ROM will also diverge from the true system response. To further improve the ROM's frequency response, nonlinear normal modes can be investigated.

In the transient wind load cases studied, the ROM exhibited strong agreement with SHARPy simulations. By retaining the quadratic nonlinearity of the FOM model, the ROM successfully captures nonlinear modal couplings in clear contrast with the LTI model. While both models were derived from the same linearization point, the ROM outperformed the LTI model in every load case studied. Among the wind load cases, the ROM's maximum out-of-plane tip deflection error was 0.77% of reference tip deflection, compared with 20.90% for the LTI model (Table 8). This improvement arises from two main factors. First, the use of intrinsic strain coordinates allows the ROM to represent large deformations more accurately than the

https://doi.org/10.5194/wes-2026-131
Preprint. Discussion started: 17 August 2026

displacement-based LTI model. Second, the ROM retains the quadratic modal couplings of the FOM, in which excitation in one direction influences the effective structural response in other directions. For instance, in the EOG case, the ROM exhibited a flattened peak in torsional tip deformations near $t = 14\ s$ (Fig. 10b), consistent with nonlinear geometric stiffening from gravity loads, while the LTI model overpredicts the response due to its inability to capture this coupling. Structural errors can also compound in the aeroelastic framework, as reflected by the aerodynamic coefficient errors of the two models at gust peak (max. error 0.37% versus 30.97%, Table 9). The nonlinear coupling effect also manifests as phase differences in the dynamic response under combined gravity and wind loading. While the ROM can capture the phase change well, the LTI model deviates from the benchmark in both phase and amplitude (Fig. 10 and Fig. 11). In the two-way aeroelastic framework, the LTI model tends to overpredict the blade deformations and aerodynamic coefficients. This can result in overcorrections by the controller during load alleviation and set-point optimization actions.

Generally, the ROM is more accurate for out-of-plane displacements than torsional deformations (max. error 0.77% versus 10.26%, Table 8). A possible cause for this behaviour is the diminished representation of torsional modes due to gyroscopic effects. For instance, mode 6, which is the first torsional mode in the stationary blade, becomes a coupled flapwise-torsional mode in the rotating blade with strong flapwise participation. Similar modal mixing is also observed in torsional modes 9, 15, and 18, to a milder degree. At increased computational cost, the representation of torsional response may be further improved by enriching the basis with modal derivatives.

7 Conclusion

This study formulated a high-fidelity ROM of the nonlinear dynamics of a wind turbine blade under unsteady and unevenly distributed wind loads. To accomplish this task, the IGEBT formulation for a spatially varying wind turbine blade was discretized using a hierarchical spectral finite element method. Then, a biorthogonal ROM was created by solving the direct and adjoint eigenvalue problems at a rotating steady state to produce a linearly independent modal basis. The biorthogonal ROM successfully captured both the frequency and time domain blade responses to external loads, in contrast with direct modes and LTI models. The biorthogonal ROM was rigorously tested using wind load cases from the IEC 61400-1 standard in a two-way aeroelastic framework. This work enables computationally efficient, high-fidelity simulation of wind turbine blade dynamics that is significantly more accurate than conventional methods. Potential applications include model predictive control design, fatigue life assessment, and digital twin development for wind farms.

Appendix A: Hierarchical Spectral Finite Element Discretization

The elemental sub-matrices $\mathbb{A}_{rs,i}$, $\mathbb{B}_{rs,i}$, $\mathbb{C}_{rst,i}$, $\mathbb{D}_{r,i}$, $\mathbb{L}_{rs,i}$, and $\mathbb{R}_{rs,i}$ are computed using hierarchical tensor notation:

$$\Psi^{V} = [\mathrm{I}_3 \quad 0 \quad 0 \quad 0], \Psi^{\Omega} = [0 \quad \mathrm{I}_3 \quad 0 \quad 0], \Psi^{\mathrm{F}} = [0 \quad 0 \quad \mathrm{I}_3 \quad 0], \Psi^{\mathrm{M}} = [0 \quad 0 \quad 0 \quad \mathrm{I}_3] \tag{A1}$$

https://doi.org/10.5194/wes-2026-131
Preprint. Discussion started: 17 August 2026

$$\begin{aligned}\mathbb{A}_{r(a)s(b),i} = \int_0^{L_i} \Big\{ &{\Psi^V_{(a)}}^T\left[\Phi_r\Phi_s G_i(x_i)\Psi^V_{(b)} + \Phi_r\Phi_s K_i(x_i)\Psi^\Omega_{(b)}\right] + {\Psi^\Omega_{(a)}}^T\left[\Phi_r\Phi_s K_i(x_i)^T\Psi^V_{(b)} + \Phi_r\Phi_s I_i(x_i)\Psi^\Omega_{(b)}\right] \\ &+ {\Psi^F_{(a)}}^T\left[\Phi_r\Phi_s R_i(x_i)\Psi^F_{(b)} + \Phi_r\Phi_s S_i(x_i)\Psi^M_{(b)}\right] \\ &+ {\Psi^M_{(a)}}^T\left[\Phi_r\Phi_s S_i(x_i)^T\Psi^F_{(b)} + \Phi_r\Phi_s T_i(x_i)\Psi^M_{(b)}\right]\Big\} dx_i\end{aligned} \tag{A2}$$

$$\begin{aligned}\mathbb{B}_{r(a)s(b),i} = \int_0^{L_i} \Big\{ &{\Psi^V_{(a)}}^T\left[-\Phi_r{\Phi_s}'\Psi^F_{(b)} - \Phi_r\Phi_s\tilde{k}_i(x_i)\Psi^F_{(b)}\right] \\ &+ {\Psi^\Omega_{(a)}}^T\left[-\Phi_r{\Phi_s}'\Psi^M_{(b)} - \Phi_r\Phi_s\tilde{k}_i(x_i)\Psi^M_{(b)} - \Phi_r\Phi_s\tilde{e_1}\Psi^F_{(b)}\right] \\ &+ {\Psi^F_{(a)}}^T\left[-\Phi_r{\Phi_s}'\Psi^V_{(b)} - \Phi_r\Phi_s\tilde{k}_i(x_i)\Psi^V_{(b)} - \Phi_r\Phi_s\tilde{e_1}\Psi^\Omega_{(b)}\right] \\ &+ {\Psi^M_{(a)}}^T\left[-\Phi_r{\Phi_s}'\Psi^\Omega_{(b)} - \Phi_r\Phi_s\tilde{k}_i(x_i)\Psi^\Omega_{(b)}\right]\Big\} dx_i + {\Psi^V_{(a)}}^T\Phi_r(L)\Phi_s(L)\Psi^F_{(b)} \\ &+ {\Psi^\Omega_{(a)}}^T\Phi_r(L)\Phi_s(L)\Psi^M_{(b)} - {\Psi^F_{(a)}}^T\Phi_r(0)\Phi_s(0)\Psi^V_{(b)} - {\Psi^M_{(a)}}^T\Phi_r(0)\Phi_s(0)\Psi^\Omega_{(b)}\end{aligned} \tag{A3}$$

$$\begin{aligned}\mathbb{C}_{r(a)s(b)t(c),i} = \int_0^{L_i} \Big\{ &{\Psi^V_{(a)}}^T\Big[\widetilde{\Psi^\Omega_{(c)}}\left(\Phi_r\Phi_s\Phi_t G_i(x_i)\Psi^V_{(b)} + \Phi_r\Phi_s\Phi_t K_i(x_i)\Psi^\Omega_{(b)}\right) - \Phi_r\Phi_s\Phi_t\left(S_\iota\widetilde{(x_\iota)^T\Psi^F_{(c)}}\right)\Psi^F_{(b)} \\ &- \Phi_r\Phi_s\Phi_t\left(T_\iota\widetilde{(x_\iota)\Psi^M_{(c)}}\right)\Psi^F_{(b)}\Big] \\ &+ {\Psi^\Omega_{(a)}}^T\Big[\widetilde{\Psi^\Omega_{(c)}}\left(\Phi_r\Phi_s\Phi_t K_i(x_i)^T\Psi^V_{(b)} + \Phi_r\Phi_s\Phi_t I_i(x_i)\Psi^\Omega_{(b)}\right) \\ &+ \widetilde{\Psi^V_{(c)}}\left(\Phi_r\Phi_s\Phi_t G_i(x_i)\Psi^V_{(b)} + \Phi_r\Phi_s\Phi_t K_i(x_i)\Psi^\Omega_{(b)}\right) - \Phi_r\Phi_s\Phi_t\left(S_\iota\widetilde{(x_\iota)^T\Psi^F_{(c)}}\right)\Psi^M_{(b)} \\ &- \Phi_r\Phi_s\Phi_t\left(T_\iota\widetilde{(x_\iota)\Psi^M_{(c)}}\right)\Psi^M_{(b)} - \Phi_r\Phi_s\Phi_t\left(R_\iota\widetilde{(x_\iota)\Psi^F_{(c)}}\right)\Psi^F_{(b)} - \Phi_r\Phi_s\Phi_t\left(S_\iota\widetilde{(x_\iota)\Psi^M_{(c)}}\right)\Psi^F_{(b)}\Big] \\ &+ {\Psi^F_{(a)}}^T\Big[-\Phi_r\Phi_s\Phi_t\left(S_\iota\widetilde{(x_\iota)^T\Psi^F_{(c)}}\right)\Psi^V_{(b)} - \Phi_r\Phi_s\Phi_t\left(T_\iota\widetilde{(x_\iota)\Psi^M_{(c)}}\right)\Psi^V_{(b)} \\ &- \Phi_r\Phi_s\Phi_t\left(R_\iota\widetilde{(x_\iota)\Psi^F_{(c)}}\right)\Psi^\Omega_{(b)} - \Phi_r\Phi_s\Phi_t\left(S_\iota\widetilde{(x_\iota)\Psi^M_{(c)}}\right)\Psi^\Omega_{(b)}\Big] \\ &+ {\Psi^M_{(a)}}^T\Big[-\Phi_r\Phi_s\Phi_t\left(S_\iota\widetilde{(x_\iota)^T\Psi^F_{(c)}}\right)\Psi^\Omega_{(b)} - \Phi_r\Phi_s\Phi_t\left(T_\iota\widetilde{(x_\iota)\Psi^M_{(c)}}\right)\Psi^\Omega_{(b)}\Big]\Big\} dx_i\end{aligned} \tag{A4}$$

$$\begin{aligned}\mathbb{D}_{r(a),i} = -\int_0^{L_i} &\left\{{\Psi^V_{(a)}}^T\Phi_r f^{grav}(x_i,t) + {\Psi^\Omega_{(a)}}^T\Phi_r m^{grav}(x_i,t)\right\} dx_i - \sum {\Psi^V_{(a)}}^T\Phi_r(x_i)F^{aero}(x_i,t) \\ &- \sum {\Psi^\Omega_{(a)}}^T\Phi_r(x_i)M^{aero}(x_i,t) - {\Psi^V_{(a)}}^T\Phi_r(L)F^{bou}(L) - {\Psi^\Omega_{(a)}}^T\Phi_r(L)M^{bou}(L) \\ &+ {\Psi^F_{(a)}}^T\Phi_r(0)V^{bou}(0) + {\Psi^M_{(a)}}^T\Phi_r(0)\Omega^{bou}(0)\end{aligned} \tag{A5}$$

$$\mathbb{L}_{r(a)s(b),i} = {\Psi^F_{(a)}}^T\Phi_r(0)\Phi_s(L_i)\Psi^V_{(b)} + {\Psi^M_{(a)}}^T\Phi_r(0)\Phi_s(L_i)\Psi^\Omega_{(b)} \tag{A6}$$

$$\mathbb{R}_{r(a)s(b),i} = -{\Psi^V_{(a)}}^T\Phi_r(L_i)\Phi_s(0)\Psi^F_{(b)} - {\Psi^\Omega_{(a)}}^T\Phi_r(L_i)\Phi_s(0)\Psi^M_{(b)} \tag{A7}$$

https://doi.org/10.5194/wes-2026-131
Preprint. Discussion started: 17 August 2026

Code and data availability

Code and data are available upon request.

Author contributions

J.X.G.: Writing -original draft, Data curation, Formal analysis, Software, Methodology, Validation, Visualization, Investigation, Conceptualization. J.E.M.: Writing – review & editing, Conceptualization, Formal analysis, Investigation, Methodology, Validation, Visualization, Supervision. D.A.R: Writing–review & editing, Formal analysis, Investigation, Validation, Visualization, Conceptualization, Supervision. C.H.A.: Writing – review & editing, Supervision, Project administration, Funding acquisition, Conceptualization, Formal analysis, Methodology, Validation, Visualization.

Competing interests

The authors declare no known financial or personal conflicts of interest that could have influenced the research presented in this manuscript.

Acknowledgements

The authors gratefully acknowledge the financial support provided by the Natural Sciences and Engineering Research Council of Canada (NSERC) for this research.

References

Alstom: Alstom inaugurates the largest offshore wind turbine in the world, near Saint-Nazaire 2012.
Althoff, M., Patil, M. J., and Traugott, J. P.: Nonlinear Modeling and Control Design of Active Helicopter Blades, J. Am. Helicopter Soc., 57, 1-11, 10.4050/jahs.57.012002, 2012.
Antonini, E. G. A., Romero, D. A., and Amon, C. H.: Optimal design of wind farms in complex terrains using computational fluid dynamics and adjoint methods, Appl. Energy, 261, 10.1016/j.apenergy.2019.114426, 2020.
Artola, M., Wynn, A., and Palacios, R.: Modal-Based Nonlinear Model Predictive Control for 3-D Very Flexible Structures, IEEE Trans. Autom. Control, 67, 2145-2160, 10.1109/tac.2021.3071326, 2022.
Baisthakur, S. and Fitzgerald, B.: Multi-task learning long short-term memory model to emulate wind turbine blade dynamics, Wind Energy Sci., 10, 1979-2004, 10.5194/wes-10-1979-2025, 2025.
Bekhoucha, F., Rechak, S., Duigou, L., and Cadou, J.-M.: Nonlinear forced vibrations of rotating anisotropic beams, Nonlinear Dyn., 74, 1281-1296, 10.1007/s11071-013-1040-3, 2013.
Berry, D. and Ashwill, T.: Design of 9-Meter Carbon-Fiberglass Prototype Blades: CX-100 and TX-100, Sandia National Laboratories, 10.2172/921145, 2007.
Dai, J., Li, M., Chen, H., He, T., and Zhang, F.: Progress and challenges on blade load research of large-scale wind turbines, Renew. Energy, 196, 482-496, 10.1016/j.renene.2022.07.017, 2022.
del Carre, A., Muñoz-Simón, A., Goizueta, N., and Palacios, R.: SHARPy: A dynamic aeroelastic simulation toolbox for very flexible aircraft and wind turbines, J. Open Source Softw., 4, 10.21105/joss.01885, 2019.

Dongfang: Major Announcement! The World's Largest 26 MW Offshore Wind Turbine Rolls Off the Line!, 2024.
Farinholt, K., Farinholt, K. M., Griffin, S. F., Taylor, S. G., Park, G., and Ammerman, C. M.: Full-scale fatigue tests of CX-100 wind turbine blades. Part I: testing, Industrial and Commercial Applications of Smart Structures Technologies 2012, 10.1117/12.917493, 2012.
Fleming, I. and Luscher, D. J.: A model for the structural dynamic response of the CX-100 wind turbine blade, Wind Energy, 17, 877-900, 10.1002/we.1603, 2013.
Genta, G.: Dynamics of Rotating Systems, Springer Science+Business Media, Inc.2005.
Gözcü, O., Barlas, E., and Dou, S.: A correction method for large deflections of cantilever beams with a modal approach, Wind Energy Sci., 8, 109-124, 10.5194/wes-8-109-2023, 2023.
GWEC: Global Wind Report 2026, Global Wind Energy Council, 2026.
Hasanpoor, S., Romero, D. A., Moran, J. E., and Amon, C. H.: Physics-informed deep convolutional hierarchical encoder-decoder neural network for flow field prediction in wind farms, Energy AI, 21, 10.1016/j.egyai.2025.100553, 2025.
Hesse, H. and Palacios, R.: Consistent structural linearisation in flexible-body dynamics with large rigid-body motion, Comput. Struct., 110-111, 1-14, 10.1016/j.compstruc.2012.05.011, 2012.
Hodges, D. H.: Geometrically Exact, Intrinsic Theory for Dynamics of Curved and Twisted Anisotropic Beams, AIAA, 10.2514/2.2054, 2003.
Hodges, D. H.: Nonlinear Composite Beam Theory, Progress in Astronautics and Aeronautics, American Institute of Aeronautics and Astronautics2006.
Jonkman, J. M., Butterfield, S., Musial, W., and Scott, G.: Definition of a 5-MW Reference Wind Turbine for Offshore System Development, National Renewable Energy LaboratoryNREL/TP-500-38060, 10.2172/947422, 2009.
Jonkman, J. M., Wright, A. D., Hayman, G. J., and Robertson, A. N.: Full-System Linearization for Floating Offshore Wind Turbines in OpenFAST, ASME 2018 1st International Offshore Wind Technical Conference, 10.1115/IOWTC2018-1025, 2018.
Machado, M. R. and Dutkiewicz, M.: Wind turbine vibration management: An integrated analysis of existing solutions, products, and Open-source developments, Energy Rep., 11, 3756-3791, 10.1016/j.egyr.2024.03.014, 2024.
Madsen, H. A., Sorensen, N., and Schreck, S.: Yaw Aerodynamics Analyzed with Three Codes in Comparison with Experiment, AIAA, 10.2514/6.2003-519, 2003.
Madsen, H. A., Riziotis, V., Zahle, F., Hansen, M. O. L., Snel, H., Grasso, F., Larsen, T. J., Politis, E., and Rasmussen, F.: Blade element momentum modeling of inflow with shear in comparison with advanced model results, Wind Energy, 15, 63-81, 10.1002/we.493, 2011.
Manolas, D. I., Riziotis, V. A., and Voutsinas, S. G.: Assessing the Importance of Geometric Nonlinear Effects in the Prediction of Wind Turbine Blade Loads, J. of Comput. and Nonlinear Dyn., 10, 10.1115/1.4027684, 2015.
Meirovitch, L.: Principles and Techniques of Vibrations, Prentice Hall1997.
Muñoz-Simón, A.: Vortex-lattice-based nonlinear aeroservoelastic modelling and analysis of large floating wind turbines, Department of Aeronautics, Imperial College London, 2021.
Muñoz-Simón, A., Wynn, A., and Palacios, R.: Unsteady and three-dimensional aerodynamic effects on wind turbine rotor loads, AIAA Scitech 2020 Forum, 10.2514/6.2020-0991, 2020.
Murua, J., Palacios, R., and Graham, J. M. R.: Applications of the unsteady vortex-lattice method in aircraft aeroelasticity and flight dynamics, Prog. Aerosp. Sci., 55, 46-72, 10.1016/j.paerosci.2012.06.001, 2012.
Palacios, R.: Nonlinear normal modes in an intrinsic theory of anisotropic beams, J. Sound Vib., 330, 1772-1792, 10.1016/j.jsv.2010.10.023, 2011.
Palacios, R. and Cesnik, C. E. S.: Dynamics of Flexible Aircraft, Cambridge University Press2023.
Pamfil, B., Bredmose, H., Kim, T., and Yu, W.: Fast response methods for aero-elastic floating wind turbine design, Wind Energy Sci., 11, 2191-2227, 10.5194/wes-11-2191-2026, 2026.
Paquette, J., Laird, D., and Griffith, D. T.: Modeling and Testing of 9m Research Blades, AIAA, 10.2514/6.2006-1199, 2011.
Patil, M.: Decoupled second-order equations and modal analysis of a general nonconservative system, 41st Structures, Structural Dynamics, and Materials Conference and Exhibit, 10.2514/6.2000-1654, 2000.
Patil, M. and Hodges, D. H.: Variable-order finite elements for nonlinear, fully intrinsic beam equation, J. Mech. Mater. Struct., 6, 479-493, 2011.

https://doi.org/10.5194/wes-2026-131
Preprint. Discussion started: 17 August 2026

Peters, N., Silva, C., and Ekaterinaris, J.: A data-driven reduced-order model for rotor optimization, Wind Energy Sci., 8, 1201-1223, 10.5194/wes-8-1201-2023, 2023.

Porte-Agel, F., Bastankhah, M., and Shamsoddin, S.: Wind-Turbine and Wind-Farm Flows: A Review, Bound. Layer. Meteorol., 174, 1-59, 10.1007/s10546-019-00473-0, 2020.

Qu, X., Li, Y., Tang, Y., Chai, W., and Gao, Z.: Comparative study of short-term extreme responses and fatigue damages of a floating wind turbine using two different blade models, Appl. Ocean Res., 97, 10.1016/j.apor.2020.102088, 2020.

Rafiee, M., Nitzsche, F., and Labrosse, M.: Dynamics, vibration and control of rotating composite beams and blades: A critical review, Thin-Walled Struct., 119, 795-819, 10.1016/j.tws.2017.06.018, 2017.

Rahimi, H., Dose, B., Stoevesandt, B., and Peinke, J.: Investigation of the validity of BEM for simulation of wind turbines in complex load cases and comparison with experiment and CFD, WindEurope Summit 2016, 10.1088/1742-6596/749/1/012015, 2016.

Reissner, E.: On One-Dimensional Large-Displacement Finite-Strain Beam Theory, Stud. Appl. Math., 52, 87-95, 10.1002/sapm197352287, 1973.

Romero, D. A., Hasanpoor, S., Antonini, E. G. A., and Amon, C. H.: Predicting wind farm wake losses with deep convolutional hierarchical encoder–decoder neural networks, APL Mach. Learn., 2, 10.1063/5.0168973, 2024.

Shabana, A. A.: Flexible Multibody Dynamics: Review of Past and Recent Developments, Multibody Syst. Dyn., 1, 189-222, 10.1023/A:1009773505418, 1997.

Siami, A. and Nitzsche, F.: A harmonic balance solution for the intrinsic 1D nonlinear equations of the beams, J. Vib. Control, 30, 1353-1367, 10.1177/10775463231162751, 2023.

Simo, J. C. and Vu-Quoc, L.: On the Dynamics in Space of Rods Undergoing Large Motions - A Geometrically Exact Approach, Comput. Methods Appl. Mech. Eng., 66, 125-161, 10.1016/0045-7825(88)90073-4, 1988.

Svendsen, M. N., Krenk, S., and Høgsberg, J.: Resonant vibration control of rotating beams, J. Sound Vib., 330, 1877-1890, 10.1016/j.jsv.2010.11.008, 2011.

Wang, Q., Johnson, N., Sprague, M., and Jonkman, J.: BeamDyn: A High-Fidelity Wind Turbine Blade Solver in the FAST Modular Framework, 33rd Wind Energy Symposium, Kissimmee, Florida, 10.2514/6.2015-1465, 2015.

Wang, Z., Hu, J., Wang, Y., Yang, M., Zhou, B., Yuan, Y., Jin, P., and Chen, Y.: Nonlinear aeroelastic performance in 5 MW and 15 MW wind turbine blades using intrinsic geometrically exact method, Renew. Energy, 256, 10.1016/j.renene.2025.124581, 2026.

Wang, Z., Hu, J., Wang, Y., Zhang, Y., Zhou, B., Jin, P., Qi, L., and Chen, Y.: Nonlinear dynamic response of long flexible wind turbine blades based on intrinsic geometrically exact theory, Energy, 338, 10.1016/j.energy.2025.138791, 2025.

Wright, A. D. and Fingersh, L. J.: Advanced Control Design for Wind Turbines Part I: Control Design, Implementation, and Initial Tests, National Renewable Energy Laboratory, 2008.

Wu, L., Tiso, P., Tatsis, K., Chatzi, E., and van Keulen, F.: A modal derivatives enhanced Rubin substructuring method for geometrically nonlinear multibody systems, Multibody Syst. Dyn., 45, 57-85, 10.1007/s11044-018-09644-2, 2019.